nature communications

Article

https://doi.org/10.1038/s41467-025-58759-6

Electronic band structure engineering of π-d conjugated metal-organic framework for sodium organic batteries

Received: 8 May 2024

Accepted: 28 March 2025

Published online: 14 April 2025

Check for updates

Juan Chu[1,2], Zhaoli Liu[1,2], Jie Yu[1], Heng-Guo Wang[1] ✉, Fengchao Cui[1] & Guangshan Zhu[1] ✉

Two-dimensional conjugated metal organic frameworks (2D c-MOFs) hold significant promise as electrode materials for alkali metal ion batteries while their electrochemical properties still lack reasonable and effective regulation. Here, two representative 2D c-MOFs (M-HHTQ/M-HHTP, M=Cu or Ni) as positive electrodes are used as models to explore the basic/microscopic principles of their complex storage mechanism in sodium ion batteries (SIBs). It is demonstrated that the energy storage mechanism of 2D c-MOFs is determined by the interaction between coordination covalent bonds and organic linkers. Theoretical calculations and experiment results have jointly demonstrated that the redox potential and theoretical capacity can be regulated based on the valence of M-O bond and the utilization of anions and cations, respectively. As a result, Cu-HHTQ achieves a high discharge voltage at 2.55 V (vs. Na^+/Na), a higher stable specific capacity of 208 mAh g^{-1} at 0.05 A g^{-1}, and long cyclability with the capacity retention rate of 100% at 1 A g^{-1} after 2000 cycles.

Two-dimensional d-π conjugated metal-organic frameworks (2D c-MOFs) have garnered considerable attention in many fields[1–5], especially alkali metal ion batteries[6–12], due to their unique crystalline structure, robust frameworks, and high chemical and thermal stabilities[13–20]. Generally, the formation of 2D c-MOFs undergoes the deprotonation, in situ oxidation, and coordination process, where ortho-substituted groups (X) of ligands are first deprotonated to form dianion and the conjugated ligands are in situ partially oxidized to form monoanionic π radical, then multi-valence transition metal ions (M) are chelated by the formed strong conjugated bases to form MX_4 building unit[21]. In this case, the unique structures and chemical states make 2D c-MOFs a meaningful model system to understand the electronic structure and multielectron-transfer mechanism. Importantly, there is a crucial relationship between their electronic structure and the electrochemical active density of states (EA-DOS)[22]. In the case of coordination frameworks, the redox of the π-d conjugated states contributed by π-electronic states (ligands) conjugating with the d-electrons (M) determines multielectron transfer (Fig. 1a), thus desirable electrochemical properties of 2D c-MOFs can be achieved by designing the electronic structure.

Similar to the transition metal ligand-based materials, the band structure consists of antibonding MX* state (d-band), purely non-bonding ligand state (p-band), and bonding MX state[23]. In electrochemical reactions, electrons transfer from the p-band of the ligand to the d-band of the metal, forming ligand holes, and then the metal is reduced. Therefore, it is of great significance to carefully select the transition metal ions and conjugated ligands that may affect the electronic/band structure for further achieving the desired electrochemical performance[24–27]. As for metal ions, the stronger the electronegativity, the stronger the oxidation ability, making them easier to get electrons and interact with cations, which is determined by the d-electrons of the transition metal itself[28–30]. In fact, the electronegativity of the conjugated ligands is also very important because it could determine the ionic and covalent character of 2D c-MOFs due to

[1]Key Laboratory of Polyoxometalate and Reticular Material Chemistry of Ministry of Education and Faculty of Chemistry, Northeast Normal University, 130024 Changchun, P. R. China. [2]These authors contributed equally: Juan Chu, Zhaoli Liu. ✉e-mail: wanghg061@nenu.edu.cn; zhugs@nenu.edu.cn

https://doi.org/10.1038/s41467-025-58759-6

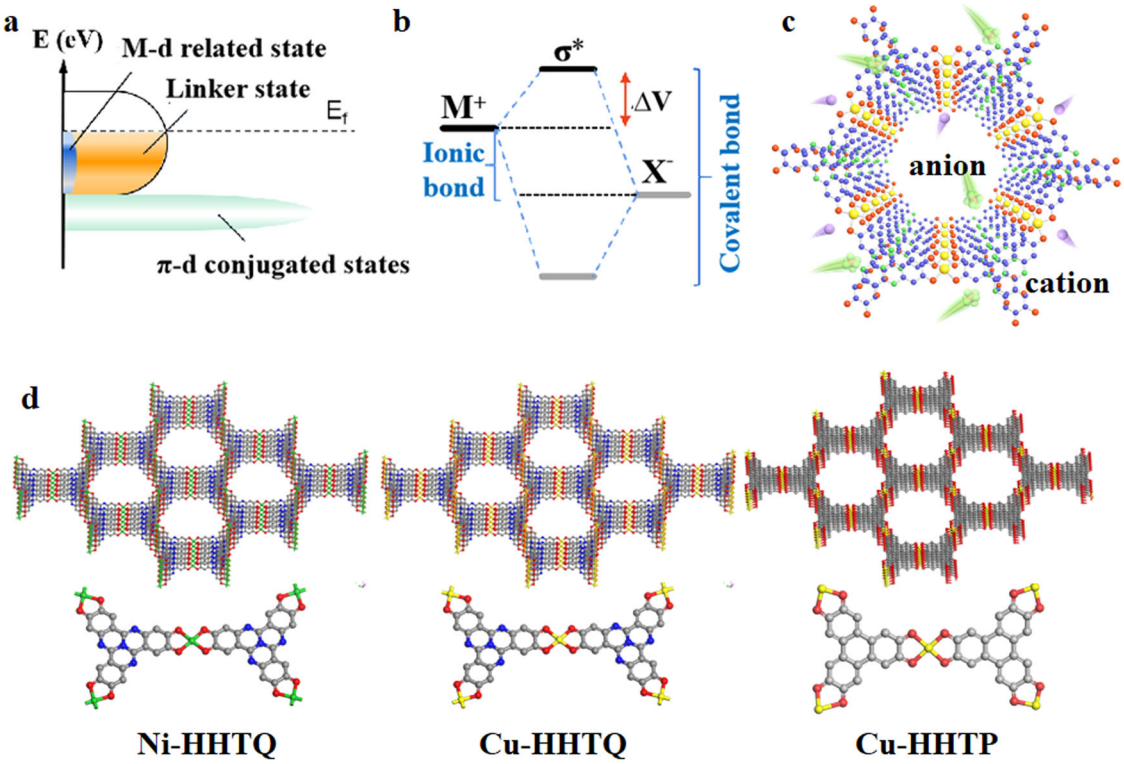

Fig. 1 | Theoretical guidance for regulating the electrochemistry of 2D c-MOFs. **a** Mechanism using the linker states and π-d conjugated states. **b** Overview of the inductive effect about the adjustment between ion and covalent characters. **c** Schematic diagram of constructing cations/anions co-storage host material. **d** Chemical structures and coordination structure around metal centers of Ni-HHTQ, Cu-HHTQ, and Cu-HHTP (Gray ball, carbon; blue ball, nitrogen; red ball, oxygen; green ball, nickel; yellow ball, copper).

the inductive effects. Covalent bonds are formed when the electronegativity of M and X are approximately equivalent, whereas ionic bonds are formed when their electronegativity is very different[31]. Thus, the inductive effect could lead to the modified local electronic properties, which drives the electrons to localize away from M, but closer to X (Fig. 1b). As a result, the increase in ionic bonds results in the reduced separation between the antibonding and bonding orbitals, thus increasing cell potential[31]. Therefore, the redox potentials could be tuned through regulating the electronegativity of ligands for 2D c-MOFs[32]. In addition, targeted regulation can be carried out on the chemical structure of ligands to utilize anions as carriers to increase the specific capacity[33]. In this context, the introduction of heteroatoms with a lone pair of electrons into the ligand can easily lose electron and interact with anions, resulting in a higher specific capacity compared to 2D c-MOFs with single active sites[20]. Therefore, the artificial bipolar 2D c-MOFs by the integration of redox-active ligand and MX_4 unit could achieve successive storage of cations and anions (Fig. 1c). Obviously, understanding the multielectron-transfer mechanism of 2D c-MOFs is of great significance and yet to be elucidated, especially from electronic band structure engineering, thus further research is highly required.

In this work, we apply 2D c-MOFs as the model to explore the multielectron-transfer mechanism from electronic band structure engineering. As a proof-of-concept demonstration of this idea, a series of 2D c-MOFs (Cu-HHTQ, Ni-HHTQ, and Cu-HHTP) (Fig. 1d) are synthesized and their electrochemical storage behaviors in sodium-ion batteries (SIBs) are investigated by systematic measurements and DFT calculations. Benefitting from the unique 2D framework, the synergistic effect of strong conjugated degree and excellent electronic structure by analyzing EA-DOS, Cu-HHTQ exhibits decent electrochemical performance, which is superior to the isostructural Ni-HHTQ and the archetypical Cu-HHTP. Furthermore, all organic SIBs (AOSIBs) paired with $Na_4C_8H_2O_6$ (NaTP) have been assembled to demonstrate the feasibility of its practical application. This work provides a new electronic engineering strategy for the microscopic understanding of the underlying multielectron-transfer mechanism and the rational design of 2D c-MOF-based electrode materials for energy-storage devices.

Results

Synthesis and characterization of M-HHTQ

M-HHTQ (M = Cu and Ni) was synthesized by the reported solvothermal reaction (Fig. 2a)[34,35]. The introduction of air atmosphere ensures the in situ oxidation of the ligand during the reaction and avoids the reduction of Cu^{2+}. To demonstrate the successful synthesis of 2D c-MOFs, a series of spectral characterizations were performed. Fourier transform infrared spectroscopy (FTIR) spectra show that the attenuate vibration peaks of O–H at around 3000 cm^{-1} confirm the deprotonation and the formation of coordination bonds between catechol ligands with metal ions, and the noticeable vibration peaks of C = O at 1632 cm^{-1} are caused by the in situ partial oxidation of the ligands (Supplementary Fig. 1). Powder X-ray diffraction (PXRD) patterns were performed to characterize the crystalline structures of M-HHTQ. The similar diffraction peaks of M-HHTQ indicate their similar arrangement motifs (Fig. 2b and Supplementary Fig. 2), in which crystalline 2D honeycomb structure shows the interlayer spacing of 3.36 Å. Their PXRD patterns fit better with the simulated ones of the eclipsed (AA) staking frameworks, which are in accordance with the reported AA-stacking pattern of Cu-HHTQ. The corresponding lattice parameters of Cu-HHTQ are $a = b = 25.80$ Å, $c = 3.36$ Å, and $\alpha = \beta = 90°$, $\gamma = 120°$. The morphologies of M-HHTQ were characterized by scanning/transmission electron microscopy (SEM/TEM). Cu-HHTQ presents very small hexagonal rod-like nanocrystals, while Ni-HHTQ shows large massive morphology formed by

https://doi.org/10.1038/s41467-025-58759-6

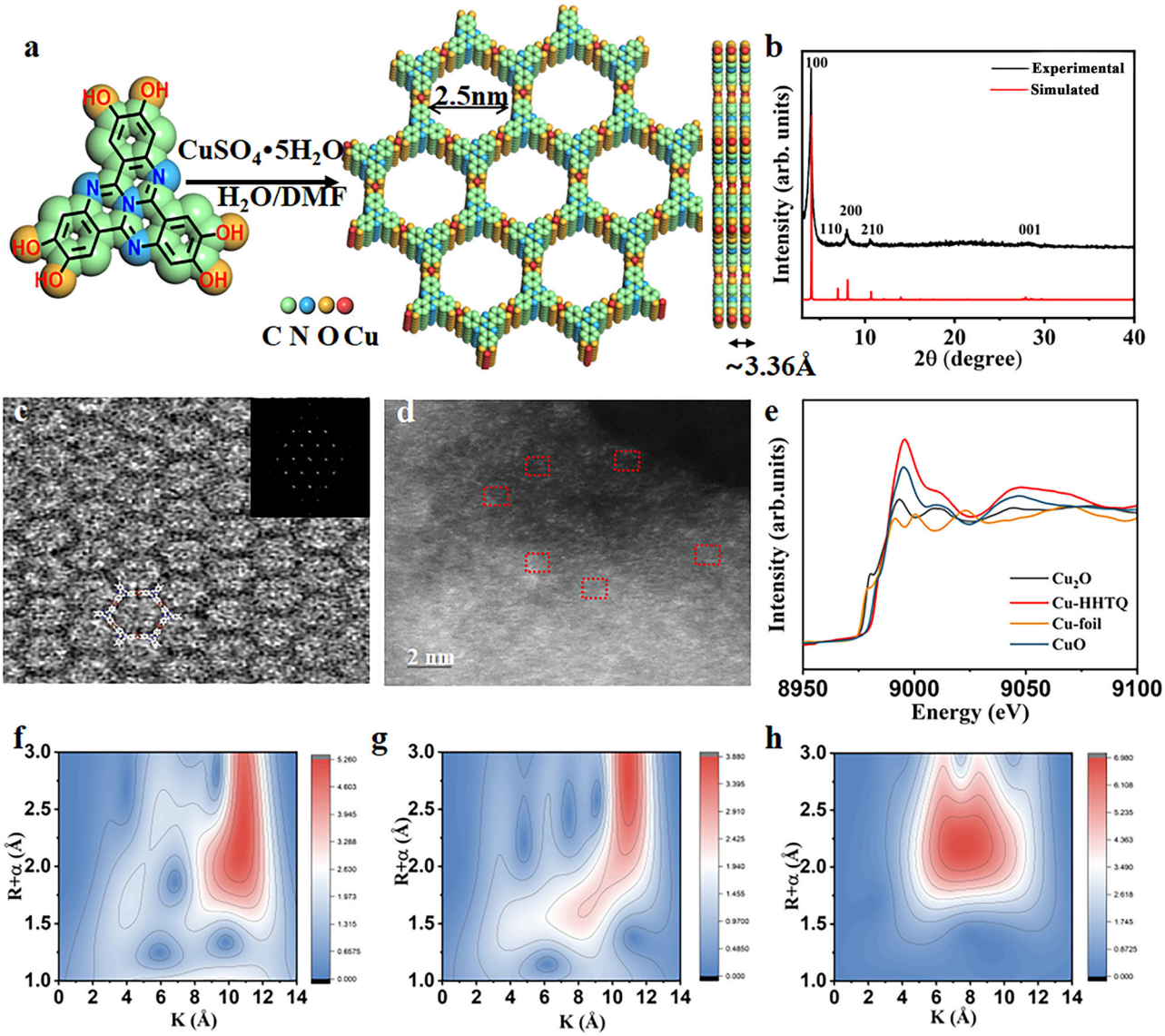

Fig. 2 | Synthesis and characterization of Cu-HHTQ. a Synthetic procedure and molecular packing of Cu-HHTQ. **b** Experimental and simulated PXRD patterns of Cu-HHTQ. **c** Zoom-in view of HRTEM image for Cu-HHTQ (the inset: FFT of the micrograph). **d** HAADF-STEM image of Cu-HHTQ. **e** XANES spectra of Cu K-edge for the standard Cu foil, Cu_2O, CuO, and Cu-HHTQ sample. Wavelet transforms of Cu-HHTQ (**f**), the standard CuO (**g**) and Cu foil (**h**) samples.

the aggregation of small base blocks, but no obvious hexagonal prism morphology was observed (Supplementary Fig. 3). HRTEM images display the visible lattice fringe of about 2.5 ± 0.2 nm for the (100) crystal plane (2θ = 4.8°) (Supplementary Fig. 4a) and the amplifying HRTEM image clearly shows the ordered honeycomb structure of Cu-HHTQ (Fig. 2c). Furthermore, HRTEM image of Cu-HHTQ also reveals the lattice distance of about 0.33 ± 0.02 nm for the interplanar distance of (001) plane resulted from the π-π stacking (Supplementary Fig. 4b). Elemental mappings reveal homogeneous distribution of C, N, O and Cu in Cu-HHTQ (Supplementary Fig. 4c). High-angle annular dark-filed scanning TEM (HAADF-STEM) image shows numerous bright dots, indicating the highly dispersed Cu species (Fig. 2d). To further elucidate the valence states of the coordination metal ions and their atomic neighborhood structures, the x-ray absorption fine structure (XAFS) spectra at the Cu K-edge was conducted. Cu-HHTQ exhibits almost the same white-line peak as CuO, indicating that Cu ions exhibit a + 2 oxidation state (Fig. 2e–h). In addition, Fourier transform (FT) spectra of extended X-ray absorption fine structure (EXAFS) oscillation $k^3\chi(k)$ for Cu-HHTQ and their corresponding fitting parameters are also given (Supplementary Fig. 5). The first coordination peak of Cu-HHTQ corresponds to the Cu-O bond at a distance of 1.98 Å, and the second coordination peak is the Cu-C interaction at a distance of 3.00 Å (Supplementary Table S1). Thus, the XAFS spectra provide ample evidence for the formation of CuO_4 groups. The pore structure of Cu-HHTQ and Ni-HHTQ were determined by the N_2 adsorption isotherm at 77 K, and the apparent Brunauer-Emmett-Teller (BET) surface area were 508 and 146.2 m^2g^{-1}, respectively (Supplementary Fig. 6). The thermal stability of M-HHTQ was evaluated by thermogravimetric analysis (TGA) (Supplementary Fig. 7), in which Cu-HHTQ and Ni-HHTQ can retain 90% of their initial mass below 300 °C, indicating the good thermal stability. In addition, from TGA curves, the proportions of Cu-HHTQ and Ni-HHTQ residues are 21.7% and 17.7%, respectively, consisting with the calculated theoretical content, which proves the successful coordination between M^{2+} and organic ligands. X-ray photoelectron spectroscopy (XPS) spectra disclose the coordination in Cu-HHTQ and Ni-HHTQ (Supplementary Fig. 8). The results show that Cu or Ni exists in the form of divalent in the M-HHTQ. In addition, Cu-HHTP for comparison has also been synthesized and characterized (Supplementary Figs. 9–14).

https://doi.org/10.1038/s41467-025-58759-6

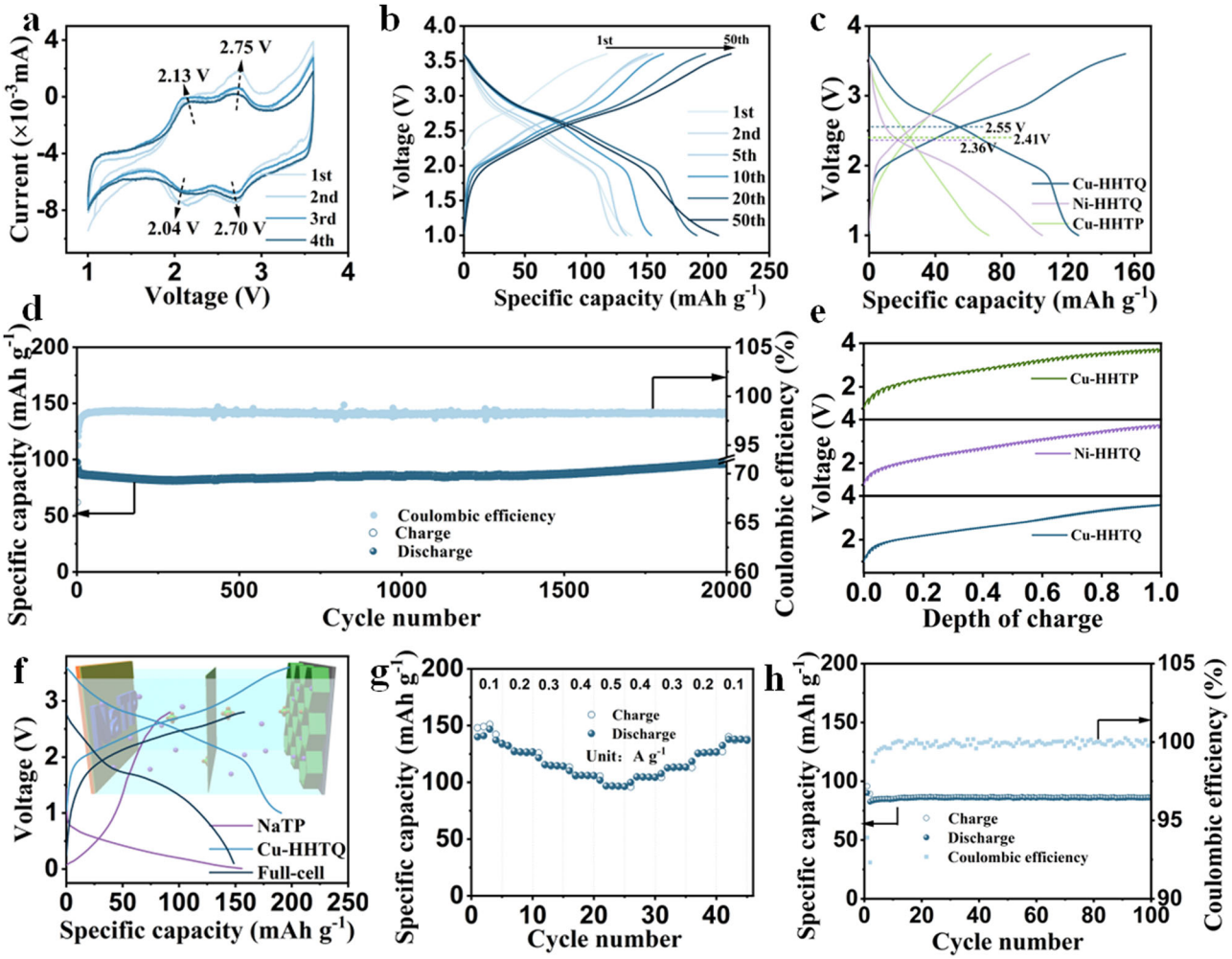

Fig. 3 | Electrochemical performance of M-HHTQ. a CV curves of Cu-HHTQ at 0.1 mV s^{-1}. **b** Galvanostatic charge/discharge curves of Cu-HHTQ and **c** the corresponding voltage profiles of Cu-HHTQ, Ni-HHTQ, and Cu-HHTP at 0.05 A g^{-1}. **d** Cycling stability of Cu-HHTQ at 1 A g^{-1}. **e** GITT curves of Cu-HHTQ, Ni-HHTQ and Cu-HHTP. **f** Charge/discharge curves of AOSIBs at 0.05 A g^{-1}. **g** Rate capability of AOSIBs at various current densities. **h** Cycling stability of AOSIBs at 1 A g^{-1}.

Electrochemical performance of M-HHTQ as the positive electrodes for SIBs

The electrochemical properties of these 2D c-MOFs as positive electrodes for SIBs were further evaluated. The increase in the content of acetylene black slightly increased the specific capacity of Cu-HHTQ, which is resulted from the increased conductivity (Supplementary Fig. 15), and fortunately, acetylene black has almost no capacity contribution (Supplementary Fig. 16). First, the cyclic voltammetry (CV) tests of Cu-HHTQ, Ni-HHTQ and Cu-HHTP were conducted in the voltage range of 1.0–3.6 V at 0.1 mV s^{-1} (Fig. 3a and Supplementary Fig. 17). However, compared to Cu-HHTQ, there is a significant difference for the CV curves of Ni-HHTQ between the first and subsequent cycles, which may be due to the higher strain/stress relaxation potential required by Ni-HHTQs in the initial cycle[36,37]. Two pairs of obvious redox peaks located at 2.13 V/2.04 V and 2.75 V/2.70 V were observed for Cu-HHTQ, respectively, corresponding to the two-step insertion of Na^+ in the electrochemical reaction. During the discharge process, the first redox reaction occurred at 2.70 V which could be a result of the conversion from Cu^{2+} to Cu^+ accompanied by an electron transfer. Followed by the discharge to 1.68 V, the unsaturated C = O double bond was reduced to a C–O single bond, which combines with Na^+. After the electrochemical activation, the overlapped CV curves indicate the reversible insertion/extraction of Na^+ in Cu-HHTQ. However, Ni-HHTQ with the same ligand as Cu-HHTQ has wider and weaker redox peaks, and relatively low oxidation potential, which may result from innocent Ni^{2+}. As for Cu-HHTP, although two pairs of redox peaks can be observed, the larger difference between the oxidation and reduction potentials shows a larger polarization voltage. The galvanostatic charge and discharge profiles of Cu-HHTQ show voltage platforms that agree well with the CV curves (Fig. 3b). To further investigate the redox process of Cu-HHTQ, differential capacity curves were obtained, in which two extra pairs of redox peaks (2.93 V/1.74 V and 3.09 V/1.46 V) may be resulted from the storage of anions (Supplementary Fig. 18). With an upward cycle trend, higher stable specific capacity of 208 mAh g^{-1} can be achieved. By contrast, Ni-HHTQ and Cu-HHTP show lower specific capacities and relatively low average discharge voltage (Fig. 3c), which can be attributed to the different electronegativity of the conjugated ligands and central metal. Furthermore, the ultra-long cycle stability test was conducted. A reversible specific capacity of 97 mAh g^{-1} with the capacity retention rate of 100% is achieved at 1 A g^{-1} after 2000 cycles (Fig. 3d). Excitingly, even at current densities of 2 and 5 A g^{-1}, Cu-HHTQ can still operate stably for 8000 and 2000 cycles without a significant capacity loss (Supplementary Fig. 19). The rate performance of Cu-HHTQ is also evaluated at current densities of 0.1–2 A g^{-1}, which can deliver a high specific capacity of 90 mAh g^{-1} at 2 A g^{-1} (Supplementary Fig. 20). When the current density gradually reduces from 2 to 0.1 A g^{-1}, a reversible capacity of 150 mAh g^{-1} almost without obvious capacity loss is

restored, which demonstrates the excellent reaction kinetics and fast electron transfer of Cu-HHTQ. Herein, Cu-HHTQ has a low Coulombic efficiency at low currents, which may be attributed to more side reactions between metal electrode and the electrolyte as well as to the formation of dendrites. However, the Joule heating generated at higher currents can self-repair dendrites[38,39]. Additionally, to comprehensively understand the fast reaction kinetics, a series of electrochemical measurements are conducted. The galvanostatic intermittent titration technique (GITT) is used to determine the ion diffusion kinetics during the electrochemical reactions (Fig. 3e and Supplementary Fig. 21). Cu-HHTQ exhibits the short spike, indicating fast equilibration and small polarization, while there are long spikes for Cu-HHTP, indicating greater polarization and slower equilibrium[31]. According to the GITT curves, the diffusion coefficients were calculated, which are 10^{-8}–10^{-10}, 10^{-10}–10^{-12} and 10^{-11}–10^{-12} $cm^2 s^{-1}$ for Cu-HHTQ, Ni-HHTQ, and Cu-HHTP, respectively (Supplementary Fig. 22), indicating the faster ion diffusion kinetics of Cu-HHTQ. The charge transfer resistance is analyzed by the electrochemical impedance spectroscopy (EIS), in which Cu-HHTQ shows lower resistance (Supplementary Fig. 23a). And as the number of cycles increases, the impedance shows a decreasing trend (Supplementary Fig. 23b), which may be due to the increase in lattice caused by repeated insertion/detachment (Supplementary Table S2), thus facilitating the migration of Na^+ ion. Furthermore, CV curves with different scan rates from 0.2 to 1 mV s^{-1} are investigated (Supplementary Figs. 24–26), in which the corresponding b values for four redox peaks of Cu-HHTQ are calculated to be 0.93, 0.96, 0.65, 0.57, respectively, which indicates that charge-storage process is controlled by Faradaic intercalation and surface pseudocapacitance. At the same time, the contribution rate of the pseudocapacitance was also calculated, and the contribution of the pseudocapacitance also increased from 44.8% to 67.6% as the scanning speed increased. The above results show the impressive electrochemical performance of Cu-HHTQ in half cells, which encourages us to assemble AOSIBs with NaTP as the negative electrodes, providing a theoretical basis for the development of practical application of 2D c-MOFs. Firstly, the voltage windows of Cu-HHTQ and NaTP were compared. Cu-HHTQ (2.55 V) has a higher discharge voltage compared to NaTP (0.4 V)[40,41], making them suitable for assembly into AOSIBs (Fig. 3f). Electrochemical sodification is achieved by discharging the NaTP to 0.01 V (vs. Na^+/Na) in a half cell at 0.05 A g^{-1}. The assembled full cell exhibits an average discharge potential of 1.6 V at a voltage window of 0.1–2.8 V and a reversible capacity of 150 mAh g^{-1} at 0.05 A g^{-1} (Supplementary Fig. 27). The rate performance of AOSIBs was evaluated between 0.1–0.5 A g^{-1} (Fig. 3g). The specific capacity of 96 mAh g^{-1} was obtained at 0.5 A g^{-1}. When the current density returns to 0.1 A g^{-1}, the specific capacity can still be maintained at 135 mAh g^{-1}. The cycle stability was evaluated at 1 A g^{-1}, the Coulombic efficiency can reach 99% with almost no capacity loss after 100 cycles (Fig. 3h). These results suggest that the Cu-HHTQ based on AOSIBs show considerable promise for practical application.

Electronic structure analysis of M-HHTQ in electrochemical reaction process

To gain a deeper understanding of why Cu-HHTQ exhibits better electrochemical performance, comprehensive theoretical calculations were conducted. The active site of MO_4 is crucial for electrochemical reaction, thus understanding the orbital interaction between M *3 d* and O *2p* is essential for elucidating the reasons. Firstly, differential charge density analysis was carried out to display the charge density distribution after the formation of MO_4 units. As observed from Supplementary Fig. 28a, b, the charge density on the Cu atoms depletes, while that on the O atoms accumulates, resulting in O atoms adopting a lower valence state, which thus is more favorable for the interaction with Na^+. In contrast, for Ni-HHTQ, there is more charge accumulation on the Ni atom, while the charge on the O atom decreases. The Cu^{2+} ion should be dsp^2-hybridized. Thus, the unpaired electron in the dx^2-y^2 orbital is to be promoted to the 4*pz* orbital with higher energy (Supplementary Fig. 28c). This potentially leads to a transfer of the electron density from the Cu^{2+} d-orbitals to the O orbital of the ligands. For Ni^{2+}, the strong-field ligand effect keeps the electrons more tightly bound in the d-orbitals, accumulating electron density at the Ni^{2+} center. The energy bands and total density of states (TDOS) of Cu-HHTQ and Ni-HHTQ were calculated using the DFT + U method (Supplementary Fig. 29). From the energy band, it can be seen that the bandgap of Cu-HHTQ is narrower than that of Ni-HHTQ, indicating an increase in electronic conductivity. Furthermore, the fully symmetric DOS of Ni-HHTQ suggests that Ni atoms lack spin states associated with unpaired electrons. Conversely, the DOS near E_f for Cu-HHTQ is asymmetric and spin polarized[27], reflecting the presence of numerous unpaired electrons on Cu atoms with the downward spin direction, consistent with that of Cu. The spin-charge density analysis reveals that the electron spin directions of Cu and O in Cu-HHTQ are aligned, whereas Ni-HHTQ lacks spin-polarized electrons (Supplementary Fig. 30). This was also corroborated by electron paramagnetic resonance (EPR) results, which exhibit a clear signal peak due to its unpaired electron while Ni-HHTQ did not present a signal peak (Supplementary Fig. 31).

A detailed analysis of the 3 d orbitals of Cu and Ni was conducted using the calculated partial density of states (PDOS). The M (II) ion coordinated with four oxygen ligands in the well-defined MO_4 active sites enables a representative square-planar crystal-field environment with a D_4h symmetry[42], where the fivefold degenerate d-bands split into three states: two twofold degenerate *dxz/dyz* and *dxy/dx²-y²* and singly degenerate *dz²*, as observed from Fig. 4a and b. Owing to the electron repulsion of axial coordination, the higher energy level of *dx²-y²* orbital decreases and degenerates with the lower energy level of *dxy* orbital (Fig. 4c)[43]. Intriguingly, such d-orbital split affects its behavior in electrochemical reaction, where Cu^{2+} can be more easily reduced to Cu^+. Furthermore, as seen in Supplementary Fig. 32, the orbitals of M (Cu and Ni) 3 d and O 2*p* form the bonding orbitals M-O and anti-bonding orbitals of M-O*. The anti-bonding orbitals of Cu-O in Cu-HHTQ are much closer to the Fermi energy level than that of Ni-O in Ni-HHTQ, indicating that Cu-HHTQ exhibits a stronger reducing property. In Cu-HHTQ, there is a significant overlap between the O 2*p* and Cu 3 *d* orbitals, which proves a strong hybridization between Cu and O, and a greater degree of electron delocalization compared to Ni-HHTQ. To further understand electron transfer during electrochemical reactions, we calculated the energy bands and DOS during the discharge process for both Cu-HHTQ and Ni-HHTQ (Supplementary Fig. 33). For Cu-HHTQ, the *dxy*, *dx²-y²* of the metal center hybridizes with O 2*px* and O 2*py* to form bonding (σ) and antibonding (σ*) orbitals (The energy of σ is relatively low and generally does not participate in chemical reactions). Upon the insertion of Na^+ into Cu-HHTQ, the electrons occupy the σ* orbital, reducing the orbital energy from 1.2 eV to 0.5 eV for Cu-HHTQ (Fig. 4d). In contrast, for Ni-HHTQ, the energy of the σ* orbital increases from 2.08 eV to 2.3 eV, which is unfavorable for electrochemical reactions (Fig. 4e). Moreover, the reduced separation between the σ and σ* orbitals enhances the electrochemical potential of the reaction, consistent with experimental results indicating that the reaction potential of Cu-HHTQ exceeds that of Ni-HHTQ. The calculated Bader charge reveals that the valence state of Cu and O decreases for each Na^+ combination during the discharge process, suggesting a significant electron transfer. However, no notable change in the valence state of Ni and O occurs during the initial step in Ni-HHTQ (Fig. 4f). Ni-HHTQ only accommodates Na^+ at a lower potential with Ni, with C = O undergoing reduction during the discharge process, explaining its lower specific capacity. Additionally, the d-π conjugation characteristics of both Cu-HHTQ and Ni-HHTQ were analyzed. Generally, the *dxz*, *dyz*, and *dz²* orbitals, which possess greater Z-direction components, align with O *pz* orbitals and hybridize side by side, forming d-π conjugates (Fig. 4g). O *pz* orbitals are continuous over a wide range and overlap well with the *dxz*, *dyz*, and *dz²* of Cu, indicating

https://doi.org/10.1038/s41467-025-58759-6

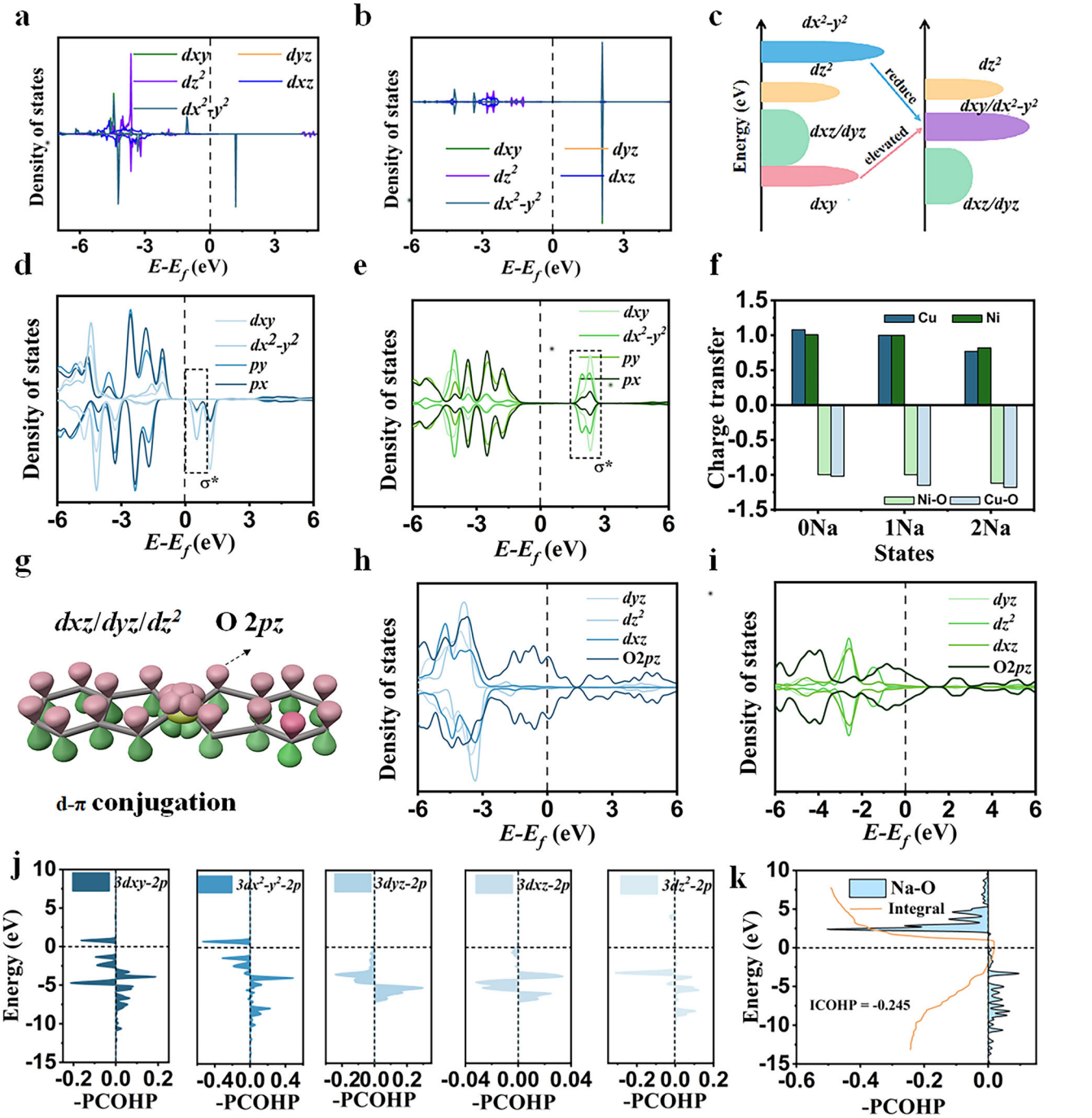

Fig. 4 | Electronic structure analysis. PDOS of (**a**) Cu-HHTQ and (**b**) Ni-HHTQ. **c** Degenerate orbital Cu-HHTQ and Ni-HHTQ. **d** PDOS of Cu-HHTQ and (**e**) Ni-HHTQ with Na^+. **f** Barder charge analysis in the electrochemical reaction process of Cu-HHTQ and Ni-HHTQ. **g** Schematic diagram of d-π conjugation. PDOS of *dxz*, *dyz*, dz^2 and O 2*pz* orbitals in (**h**) Cu-HHTQ and (**i**) Ni-HHTQ. **j** PCOHP analysis of Cu-O bond in Cu-HHTQ with Na^+. **k** PCOHP of Na-O bond in Cu-HHTQ and the integrated COHP (ICOHP) value of Na-O bond.

effective delocalization of π electrons, which facilitates continuous electron conduction. In contrast, the O *pz* orbitals in the Ni-HHTQ are discontinuous, indicating partial π electrons localization, which hampers electron conduction (Fig. 4h, i). The bonding/antibonding properties in electronic states were quantitatively assessed using the Projected Crystal Orbital Hamiltonian Population (PCOHP) (Fig. 4j and Supplementary Fig. 34). The calculation results before and after the Na^+ binding suggest that the primary participating orbitals are *dxy*, dx^2-y^2, and *dxz* during the discharge process. The energies of the original *dxy*, dx^2-y^2 orbitals decrease, while the previously unoccupied *dxz* antibonding orbitals transition to occupied states. For Ni-HHTQ, the interaction among electrons intensifies during electrochemical reaction, leading to increased localization of electrons and subsequent splitting of the *dxy* orbitals. This splitting results in the emergence of new energy levels in the band structure, creating a new band gap that restricts electron transfer (Supplementary Fig. 35). The more negative integrated COHP (ICOHP) value (−0.245) of Na-O bonding up to the Fermi level for Cu-HHTQ suggests a stronger coupling of Na^+ compared to Ni-HHTQ (−0.235) (Fig. 4k and Supplementary Fig. 36)[44]. In consequence, analyzing DOS reveals that Cu-HHTQ, characterized by low antibonding orbitals and continuous d-π conjugation, demonstrate higher discharge voltage and specific capacity compared to Ni-

HHTQ, paving the way for precise modulation of the properties of 2D c-MOFs as positive electrodes for SIBs.

Charge storage mechanism and ion diffusion analysis of M-HHTQ

To gain a deeper understanding of the working principle of Cu-HHTQ, a series of ex-situ characterizations have been applied. Firstly, ex-situ FTIR spectra were used to monitor the changes in chemical functional groups of the Cu-HHTQ during cycling (Supplementary Fig. 37). After deep discharge to 1.0 V, the peak intensity of C = O at 1636 cm^{-1} gradually weakens, while the peak intensity of C–O at 1250 cm^{-1} increases, indicating a transition between the C = O group and the C-O group[45,46]. At the same time, when charged to 3.6 V, the characteristic peak at 800–1000 cm^{-1} shows significant enhancement, which further proves the embedding of PF_6^- in the charging process. Furthermore, XPS was used to evaluate the valence state changes at different potentials (Supplementary Fig. 38). The valence states of copper in the pristine Cu-HHTQ are all +2, and when discharged to 1.0 V, it is evident that some Cu^{2+} is reduced to Cu^+, and when charged to 3.6 V, Cu^+ disappears. To record the changes in electron numbers of Cu-HHTQ during cycling, ex-situ EPR was conducted. The EPR signal intensity of the Cu-HHTQ decreases when discharged to 1.0 V, followed by a significant increase in further charging to 3.6 V, indicating the conversion of C = O bonds (or C-O radical, semi-quinone chemical state) to C-O bonds (all C = O bonds become a single bond after discharge) (Supplementary Fig. 39). To investigate the changes in the crystal structure of Cu-HHTQ during charging and discharging processes, ex-situ XRD tests were executed. The XRD patterns show that the peak positions are significantly shifted during the charging process, which agrees with the theoretical calculations (Supplementary Fig. 40). Whereas, the peaks returned to their original positions during the discharge process, which fully demonstrated the reversibility of the electrochemical reaction and the reversible insertion and detachment of anions in the Cu-HHTQ lattice. In addition, in situ Raman spectroscopy also confirmed the structural integrity and reversible changes of Cu-HHTQ during the charge/discharge processes (Supplementary Fig. S41). Further, Ab initio molecular dynamics (AIMD) calculations also demonstrated the restoration of the structure after the deintercalation of PF_6^- (Supplementary Video S1). Although the layered structure exhibits bending and rippling upon the PF_6^- intercalation within a reasonable range, the layered structure could gradually return to near the original state after the PF_6^- deintercalation. Furthermore, the distance of Cu–O bonds after the PF_6^- deintercalation was also monitored (Supplementary Fig. 42), which displayed that the distance of Cu–O coordination bonds varied in the range of 1.8–2.2 nm, while the theoretical Cu–O coordination bond was 1.92–2.37 nm, further evidencing that the structure in the plane is stable during the intercalation and deintercalation of PF_6^-.

To further explore the reaction mechanism of Cu-HHTQ, DFT was conducted to calculate the binding energy and embedding potential of Na^+. According to the discharge platform of the discharge curve, the electron transfer numbers of the three platforms are 2, 3 and 3, respectively, corresponding to the absorption of $2PF_6^-$, $3Na^+$, and $3Na^+$, contributing to the specific capacities of 53 mAh g^{-1}, 79 mAh g^{-1}, and 75 mAh g^{-1} (Fig. 5a). The calculated redox potential of Cu-HHTQ shows that the embedding potential of PF_6^- is about 3 V (Fig. 5b). Based on the previous assumption that the introduction of N in the ligand can lose electrons and bind to PF_6^-, the binding energy of PF_6^- was calculated to be 2.99 V, contributing the specific capacity of 52.9 mAh g^{-1}. Next, the binding sites and binding energy of Cu-HHTQ and Na^+ were calculated. Firstly, the Cu^{2+} in the CuO_4 unit receives an electron and combines with Na^+, resulting in a calculated potential of 2.83 V, theoretically contributing to the theoretical capacity of 80 mAh g^{-1}, which is consistent with the experimental results. Then, Na^+ combines with the O atom in the unit of CuO_4, and the oxidation–reduction potential is 1.84 V. The spin-charge density of Cu-HHTQ and Ni-HHTQ was analyzed during the discharging process, and there was no significant change in Cu-HHTQ before and after the electrochemical reaction (Fig. 5c). Na^+ mobility in electrode materials has a great influence on rate performance, so it is calculated for two representative paths P1 and P2. P1 represents the intralayer diffusion of Na^+ ions from the "a" site to the "g" site, while P2 represents the interlayer diffusion of Na^+ ions from the "a" site to the "g" site (Fig. 5d, f). Figure 5e, g represents the diffusion energy barriers of Na^+ along the two paths, clearly indicating that the energy barrier of 0.46 eV for diffusion along the P1 path is much lower than 2.1 eV of intralayer diffusion. This may be due to the small interlayer spacing, which makes it difficult for Na^+ migration.

Discussion

In summary, we report a strategy for exploring the multielectron-transfer mechanism from electronic band structure engineering by using the 2D c-MOF (Cu-HHTQ) as a proof-of-concept. Different from its counterpart 2D c-MOF Ni-HHTQ and Cu-HHTP, Cu-HHTQ features stronger electronegativity, stronger conjugated degree and excellent electronic structure by analyzing EA-DOS, contributing to the increasing cell potential, specific capacity, and reaction kinetics. Consequently, Cu-HHTQ displayed a high discharge voltage at 2.55 V (Na^+/Na), a higher stable specific capacity of 208 mAh g^{-1} at 0.05 A g^{-1}, and remarkable cyclability with the capacity retention rate of 100% at 1 A g^{-1} after 2000 cycles. As a result, the Cu-HHTQ//NaTP AOSIBs also show a reversible capacity of 150 mAh g^{-1} at 0.05 A g^{-1} and good cyclability. These results emphasize the importance of bipolar active sites in Cu-HHTQ and deepen the understanding and precise regulation of its microscopic working mechanism, which provides a feasible scheme for the design and development of high-performance positive electrodes for SIBs in the future by regulation of electronic band structure.

Methods

Materials

All solvents and chemicals were of analytical grade and used without further purification. HHTQ = 2,3,7,8,12,13-Hexahydroxytricycloquinazoline (99%, Jilin Chinese Academy of Sciences-Yanshen Technology Co., Ltd.), $CuSO_4{\cdot}5H_2O$ (99%, Aladdin), $Ni(OAc)_2{\cdot}4H_2O$ (99%, Aladdin), $Cu(OAc)_2$ (98%, Aladdin), Electrolyte (1 M $NaPF_6$ in DME, DoDoChem), Na metal (Purity 99.75%, thickness 0.5 mm, diameter 14 mm, DoDoChem), Separator (GF/6227, thickness 0.62 ± 0.01 mm, average Pore diameter 2.76 um DoDoChem), PVDF (Electronic grade, Aladdin), NMP (Electronic grade, Aladdin).

Synthesis of M-HHTQ. HHTQ (50 mg, 0.12 mmol) was placed in a 10 mL scintillation vial, and 1 mL of *N, N*-dimethylformamide (DMF) was added. The vial was subjected to ultrasonication until the ligand was completely dissolved in DMF. Subsequently, a solution of $CuSO_4{\cdot}5H_2O$ (45 mg, 0.18 mmol) in 2 mL of deionized water was added to the vial. The resulting mixture was ultrasonicated for 5 min. The vial was then sealed and heated at 85 °C for 24 h. After the reaction, the resulting black powder was collected by suction filtration using a nylon membrane and washed sequentially with DMF, deionized water, ethanol, and acetone. The final product was dried under vacuum at 120 °C overnight[34].

A solution of $Ni(OAc)_2{\cdot}4H_2O$ (22.5 mg, 0.09 mmol) in 3 mL of water was prepared and added to a solution of HHTQ (12.48 mg, 0.03 mmol) in 1 mL of DMF. The mixture was subjected to ultrasonication in a vial for 30 min, followed by heating in an oven at 85 °C for 72 h. After the reaction, the resulting black powder was collected by centrifugation and washed repeatedly with water and acetone. The product was then dried overnight under a vacuum at 120 °C[35].

Synthesis of Cu-HHTP. The HHTP ligand (97.2 mg, 3 mmol) was dispersed in 10 mL of isopropanol using ultrasound. To this dispersion, 10 mL of an aqueous solution containing $Cu(OAc)_2$ (88.9 mg,

https://doi.org/10.1038/s41467-025-58759-6

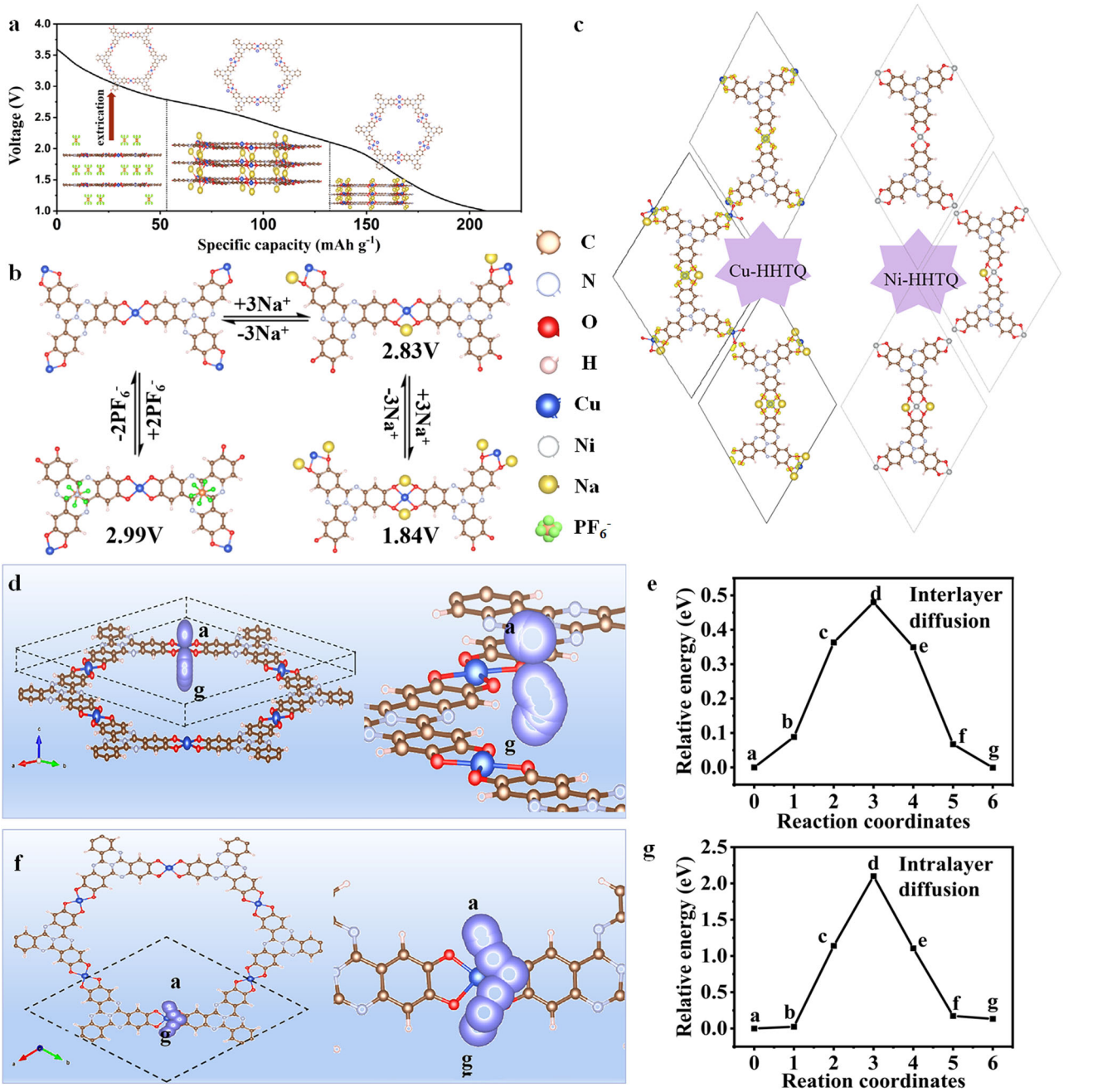

Fig. 5 | The charge storage mechanism of MOF-HHTQ. a Three-step anion and cation co-storage mechanism for Cu-HHTQ. **b** The simulated voltage platforms of Cu-HHTQ. **c** The changes in spin-charge density of Cu-HHTQ and Ni-HHTQ during the discharging process. **d** Schematic showing the P1 diffusion path and (**e**) corresponding diffusion energy barrier. **f** Schematic showing the P2 diffusion path and (**g**) corresponding diffusion energy barrier.

4.9 mmol) was added dropwise. The resulting mixture was stirred for 15 min under ambient conditions. After stirring, the mixture was transferred to an autoclave and heated at 85 °C for 15 h in a preheated oven. The final product was collected by filtration and sequentially washed with water, ethanol, and acetone[36].

Assembly of half-cell of SIBs. In the fabrication of half-cell, the positive electrodes were prepared by mixing active materials (Cu-HHTQ, Ni-HHTQ or Cu-HHTP), acetylene black, and polyvinylidene fluoride (PVDF) in a ratio of 4:5:1 or 6:3:1 with an appropriate amount of *N*-methylpyrrolidone (NMP) (Except where noted, electrochemical tests were performed with electrode composition of 4:5:1). Then, the uniform slurry was cast on aluminum foil and dried at 80 °C for 12 h. The active substance loading of each electrode was controlled at 1.0–1.2 mg/cm^2. The electrode was cut into circular discs with a diameter of 12 mm. CR2032-type coin cells were assembled by coupling the above positive electrodes with the commercial Na sheet using the glass fiber as the separator and 1 M $NaPF_6$ in DME as the electrolyte.

Assembly of full-cell of AOSIBs. The assembly of full-cell uses pre-sodification NaTP as the negative electrodes and Cu-HHTQ as the positive electrodes. The NaTP was made by grinding NaTP, acetylene black, and PVDF in the ratio of 7:2:1 in an appropriate amount of NMP, and the black slurry obtained was coated on copper foil. The mass ratio of the positive electrodes and negative electrodes is about 1.2:1, and the mass of the positive electrodes is used as the active substance mass. Before assembling the full-cell of AOSIBs, the pre-sodification of NaTP was performed. The electrochemical test of full battery is

conducted within the voltage range of 0.1-2.8 V. For the ex-situ testing of Cu-HHTQ electrodes, the Cu-HHTQ electrodes in various states were collected in an argon-filled glove box, carefully sealed, and protected from air exposure during sample transportation. For the in situ testing, the Cu-HHTQ electrode was assembled into a tightly sealed in situ cell within the glove box, followed by subsequent testing.

Electrochemical measurements. The galvanostatic charge/discharge tests were performed at different current densities within a potential of 1–3.6 V or 0.1–2.8 V on a LAND-CT3001A battery testing instrument (LAND Electronic Co., Wuhan China) at 25 °C (Concerning the repeatability of the battery, we performed three replicate experiments, maintaining the experimental error within a 10% margin. The specific analytical methodology is detailed in Supplementary Fig. S43). CV measurements were carried out in the different scan rates within a potential of 1-3.6 V using CHI760 Workstation. Electrochemical impedance spectra (EIS) were carried out on CHI760 Workstation in a frequency range of 0.01–100,000 Hz.

Material characterizations. The Fourier Transform Infrared (FTIR) spectra were recorded in the region of 400–4000 cm^{-1} on a Nicolet Magna 560IR spectrometer. Scanning electron microscopy (SEM) images were performed on a JEOS JSM 6700. ^1H NMR was measured on Bruker 500 M (Bruker, Germany) with (methyl sulfoxide)-d_6 as the solvent. Thermogravimetric analysis (TGA) was performed using a Perkin-Elmer TGA analyzer system at a heating rate of 10 °C min^{-1} in air. Powder X-ray diffraction (PXRD) was performed with a Siemens D5005 diffractometer with scanning rate of 1 ° min^{-1} (2θ). The gas adsorption-desorption isotherms were measured on a Quantachrome Autosorb-iQ_2 analyzer. Surface areas and was measured via a Specific surface area and pore size analyzer (ipore 600) by drying samples at 100 °C for 8 h under vacuum (10^{-5} bar) before analysis, and pore size distribution was calculated by nonlocal density functional theory (NLDFT). High-resolution transmission electron microscopy (HRTEM) images were collected on an FEI TALOS-200X transmission electron microscope under the accelerating voltage of 200 kV. X-ray photoelectron spectrometer (XPS, AXIS Ultra DLD) was utilized to study the surface chemistry of the samples. HAADF-STEM images were recorded on a JEOL-2100F FETEM with an electron acceleration energy of 200 kV. The X-ray absorption fine structure (XAFS) spectra were collected by easyXAFS300+.The Raman spectra were collected using a HORIBA LabRAM Odyssey instrument.

Theoretical calculation. The simulations were performed with the periodic plane-wave implementation of density functional theory (DFT) in the Vienna Ab initio Simulation Package (VASP)[47]. Blochl's projector augmented wave (PAW) method was used to describe core-valence interaction with a plane wave cut-off energy of 450 eV[48]. Spin polarization calculations performed for all simulations with the consideration of empirical dispersions of Grimme (DFT-D3) for the long-range vdW interactions. Hubbard U correction in the form of GGA + U was applied to compute on Cu (U = 7.0 eV, J = 0 eV) and Zn (U = 7.0 eV, J = 0 eV) surfaces. Brillouin-zone integrations were applied with k-point sampling of the Monkhorst–Pack scheme in a 2 × 2 × 5 grid with accuracy levels of 0.03 instructure optimization. The convergence criterion of energy and structural relaxation were 1.0 × 10^{-5} eV and 0.04 eV/Å, respectively. To quantitatively describe the diffusion behavior of Na^+ ion, we further obtained minimal energy path profiles using the nudged elastic band (NEB) method. Ab initio molecular dynamics (AIMD) simulations were performed using the PBE functional and the PAW pseudopotential. Brillouin-zone integrations were applied with k-point sampling of the Gamma scheme in a 1 × 1 × 1 grid. AIMD simulations in the NpT ensemble lasted 1.5 ps with a time step of 1 fs. The temperature of the AIMD was maintained at 300 K using the Langevin method. In order to facilitate the de-insertion of PF_6^-, we applied a pressure of 1 bar in the Z direction.

Reporting summary

Further information on research design is available in the Nature Portfolio Reporting Summary linked to this article.

Data availability

The data that support the findings of this study are available within the article (and its Supplementary Information files) and from the corresponding authors upon request.

References

1. Xie, L., Skorupskii, G. & Dincă, M. Electrically conductive metal-organic frameworks. *Chem. Rev.* **120**, 8536–8580 (2020).
2. Wang, M., Dong, R. & Feng, X. Two-dimensional conjugated metal-organic frameworks (2D c-MOFs): chemistry and function for MOFtronics. *Chem. Soc. Rev.* **50**, 2764–2793 (2021).
3. Shang, S. et al. A one-dimensional conductive metal-organic framework with extended π-d conjugated nanoribbon layers. *Nat. Commun.* **13**, 7599 (2022).
4. Huang, X. et al. A two-dimensional π-d conjugated coordination polymer with extremely high electrical conductivity and ambipolar transport behaviour. *Nat. Commun.* **6**, 7408 (2015).
5. Ross, R. et al. Operando elucidation of electrocatalytic and redox mechanisms on a 2D metal organic framework catalyst for efficient electrosynthesis of hydrogen peroxide in neutral media. *J. Am. Chem. Soc.* **144**, 15845–15854 (2022).
6. Lv, Q., Zhu, Z., Ni, Y., Geng, J. & Li, F. Spin-state manipulation of two-dimensional metal-organic framework with enhanced metal-oxygen covalency for lithium oxygen batteries. *Angew. Chem. Int. Ed.* **61**, e202114293 (2022).
7. Wang, L. et al. A two-dimensional metal-organic polymer enabled by robust, nickel-nitrogen and hydrogen bonds for exceptional sodium-ion storage. *Angew. Chem. Int. Ed.* **59**, 22126–22131 (2020).
8. Wang, J. et al. Anchoring π-d conjugated metal-organic frameworks with dual-active centers on carbon nanotubes for advanced potassium-ion batteries. *Adv. Mater.* **36**, 2305605 (2024).
9. Chen, Y. et al. A one-dimensional π-d conjugated coordination polymer for sodium storage with catalytic activity in Negishi coupling. *Angew. Chem. Int. Ed.* **131**, 14873–14881 (2019).
10. Jiang, Q. et al. A redox-active 2d metal-organic framework for efficient lithium storage with extraordinary high capacity. *Angew. Chem. Int. Ed.* **132**, 5311–5315 (2020).
11. Fang, C. et al. A metal-organic compound as cathode material with superhigh capacity achieved by reversible cationic and anionic redox chemistry for high-energy sodium-ion batteries. *Angew. Chem. Int. Ed.* **129**, 6897–6901 (2017).
12. Wang, F. et al. Fully conjugated phthalocyanine copper metal-organic frameworks for sodium-iodine batteries with long-time-cycling durability. *Adv. Mater.* **32**, 1905361 (2020).
13. Zhang, J. et al. Two-dimensional conjugated metal-organic framework with metallic charge transport. *J. Am. Chem. Soc.* **145**, 23630–23638 (2023).
14. Lu, Y. et al. Tunable charge transport and spin dynamics in two-dimensional conjugated metal-organic frameworks. *J. Am. Chem. Soc.* **146**, 2574–2582 (2024).
15. Yu, M., Dong, R. & Feng, X. Two-dimensional carbon-rich conjugated frameworks for electrochemical energy applications. *J. Am. Chem. Soc.* **142**, 12903–12915 (2020).
16. Zhang, P. et al. Largely pseudocapacitive two-dimensional conjugated metal-organic framework anodes with lowest unoccupied molecular orbital localized in nickel-bis(dithiolene) linkages. *J. Am. Chem. Soc.* **145**, 6247–6256 (2023).

17. Chakraborty, G., Park, I., Medishetty, R. & Vittal, J. Two-dimensional metal-organic framework materials: synthesis, structures, properties and applications. *Chem. Rev.* **121**, 3751–3891 (2021).
18. Debela, T. et al. Ligand-mediated hydrogenic defects in two-dimensional electrically conductive metal-organic frameworks. *J. Am. Chem. Soc.* **145**, 11387–11391 (2023).
19. Meng, Z. et al. Hierarchical tuning of the performance of electrochemical carbon dioxide reduction using conductive two-dimensional metallophthalocyanine based metal-organic frameworks. *J. Am. Chem. Soc.* **142**, 21656–21669 (2020).
20. Qi, M. et al. A rhombic 2d conjugated metal–organic framework as cathode for high-performance sodium-ion battery. *Adv. Mater.* **36**, 2401878 (2024).
21. Dou, J. et al. Atomically precise single-crystal structures of electrically conducting 2D metal-organic frameworks. *Nat. Mater.* **20**, 222–228 (2021).
22. Sakaushi, K. & Nishihara, H. Two-dimensional π-conjugated frameworks as a model system to unveil a multielectron-transfer-based energy storage mechanism. *Acc. Chem. Res.* **54**, 3003–3015 (2021).
23. Grimaud, A., Hong, W., Shao-Horn, T. & Tarascon, J. Anionic redox processes for electrochemical devices. *Nat. Mater.* **15**, 121–126 (2016).
24. Ni, Y. et al. Regulating electrocatalytic oxygen reduction activity of metal coordination polymer via d-π conjugation. *Angew. Chem. Int. Ed.* **60**, 16937–16941 (2021).
25. Wang, Y. et al. Boosting the reversibility and kinetics of anionic redox chemistry in sodium-ion oxide cathodes via reductive coupling mechanism. *J. Am. Chem. Soc.* **145**, 22708–22719 (2023).
26. Yahia, M., Vergnet, J., Saubanère, M. & Doublet, M. Unified picture of anionic redox in Li/Na-ion batteries. *Nat. Mater.* **18**, 496–502 (2019).
27. Lv, Q. et al. Atomic ruthenium-riveted metal-organic framework with tunable d-band modulates oxygen redox for lithium-oxygen batteries. *J. Am. Chem. Soc.* **144**, 23239–23246 (2022).
28. Xin, H. et al. Effects of d-band shape on the surface reactivity of transition-metal alloys. *Phys. Rev. B* **89**, 115114 (2014).
29. Dompablo, M., Armand, M., Tarascon, J. & Amador, U. On-demand design of polyoxianionic cathode materials based on electronegativity correlations: an exploration of the Li_2MSiO_4 system (M = Fe, Mn, Co, Ni). *Electrochem. Commun.* **8**, 1292–1298 (2006).
30. Li, C., Geng, F., Hu, B. & Hu, B. Anionic redox in na-based layered oxide cathodes: a review with focus on mechanism studies. *Mater. Today Energy* **17**, 100474 (2020).
31. Melot, B. & Tarascon, J. Design and preparation of materials for advanced electrochemical storage. *Acc. Chem. Res.* **46**, 1226–1238 (2013).
32. Muraliganth, T. & Manthiram, A. Understanding the shifts in the redox potentials of olivine LiM1-yMyPO4 (M) Fe, Mn, Co, and Mg) solid solution cathodes. *J. Phys. Chem. C* **114**, 15530–15540 (2010).
33. Sun, W. et al. Ion Co-storage in porous organic frameworks through onsite coulomb interactions for high energy and power density batteries. *Angew. Chem. Int. Ed.* **62**, e20230015 (2023).
34. Yan, J. et al. Immobilizing redox-active tricycloquinazoline into a 2d conductive metal–organic framework for lithium storage. *Angew. Chem. Int. Ed.* **60**, 24467–24472 (2021).
35. Liu, J. et al. Tricycloquinazoline-based 2d conductive metal-organic frameworks as promising electrocatalysts for CO_2 reduction. *Angew. Chem. Int. Ed.* **60**, 14473–14479 (2021).
36. Chen, Y. et al. Successive storage of cations and anions by ligands of π-d conjugated coordination polymers enabling robust sodium-ion batteries. *Angew. Chem. Int. Ed.* **60**, 18769–18776 (2021).
37. Tang, M. et al. Tailoring p-conjugated systems: from π-π stacking to high-rate-performance organic cathodes. *Chem* **4**, 2600–2614 (2018).
38. Tang, M. et al. Small amount COFs enhancing storage of large anions. *Energy Storage Mater.* **27**, 35–42 (2020).
39. Li, L. et al. Self-heating-induced healing of lithium dendrites. *Science* **359**, 1513–1516 (2018).
40. Wang, S. et al. All organic sodium-ion batteries with $Na_4C_8H_2O_6$. *Angew. Chem. Int. Ed.* **126**, 6002–6006 (2014).
41. Banda, H., Damien, D., Nagarajan, K., Hariharanb, M. & Shaijumon, M. A polyimide based all-organic sodium ion battery. *J. Mater. Chem. A* **3**, 10453–10458 (2015).
42. Dai, Y. et al. Tailoring the d-orbital splitting manner of single atomic sites for enhanced oxygen reduction. *Adv. Mater.* **35**, 2210757 (2023).
43. Jia, K. et al. Long-life regenerated $LiFePO_4$ from spent cathode by elevating the d-band center of Fe. *Adv. Mater.* **35**, 2208034 (2023).
44. Lao, Z. et al. Band structure engineering and orbital orientation control constructing dual active sites for efficient sulfur redox reaction. *Adv. Mater.* **36**, 2309024 (2024).
45. Fan, K., Zhang, C., Chen, Y., Wu, Y. & Wang, C. The chemical states of conjugated coordination polymers. *Chem* **7**, 1224–1243 (2021).
46. Liu, Y. et al. Activating aromatic rings as Na-ion storage sites to achieve high capacity. *Chem* **4**, 2463–2478 (2018).
47. Kresse, G. & Furthmüller, J. Efficiency of ab-initio total energy calculations for metals and semiconductors using a plane-wave basis set. *Comp. Mater. Sci.* **6**, 15–50 (1996).
48. Blöchl, P. E. Projector augmented-wave method. *Phys. Rev. B* **50**, 17953–17979 (1994).

Acknowledgements

This work is financially supported by the National Natural Science Foundation of China (Grant No. 52172186, 22479023; H. G. Wang and U21A20330; G. Zhu), the Science & Technology Department of Jilin Province (20230508057RC; H. G. Wang). The authors sincerely thank Prof. Daliang Zhang at Chongqing University for supplying high-resolution electron microscopy tests.

Author contributions

J.C. and Z.L. contributed equally to this work. H.G.W. and G.Z. supervised and designed the experiments. J.C. prepared the electrode materials, performed the electrochemical and characterization tests, analyzed the data and wrote the draft manuscript. Z.L. performed the theoretical calculation. H.G.W. and G.Z. revised the manuscript. J.Y. assisted with analyzing the experimental and characterization data. F.C. assisted with performing the theoretical calculation. All authors contributed to the discussion and preparation of this paper.

Competing interests

The authors declare no competing interests.

Additional information

Supplementary information The online version contains supplementary material available at https://doi.org/10.1038/s41467-025-58759-6.

Correspondence and requests for materials should be addressed to Heng-Guo Wang or Guangshan Zhu.

Peer review information *Nature Communications* thanks Christopher Hendon, and the other, anonymous, reviewers for their contribution to the peer review of this work. A peer review file is available.